



Ruan, S., Qiu, J., Yang, E.-H. and Unluer, C. (2021) Influence of crack width on the stiffness recovery and self-healing of reactive magnesia-based binders under CO₂-H₂O conditioning. *Construction and Building Materials*, 269, 121360.

There may be differences between this version and the published version. You are advised to consult the publisher's version if you wish to cite from it.

<http://eprints.gla.ac.uk/234406/>

Deposited on: 17 February 2021

Enlighten – Research publications by members of the University of Glasgow
<http://eprints.gla.ac.uk>

1 **Influence of crack width on the stiffness recovery and self-healing of**
2 **reactive magnesia-based binders under CO₂-H₂O conditioning**

3
4 Shaoqin Ruan^{a,b}, Jishen Qiu^{b,c}, En-Hua Yang^b, Cise Unluer^{d,*}

5
6 ^a College of Civil Engineering and Architecture, Zhejiang University, Hangzhou,
7 310058, PR China

8 ^b School of Civil and Environmental Engineering, Nanyang Technological
9 University, 50 Nanyang Avenue, Singapore 639798, Singapore

10 ^c Department of Civil and Environmental Engineering, Hong Kong University of
11 Science and Technology, Hong Kong SAR, PR China

12 ^d School of Engineering, University of Glasgow, G12 8LT, Glasgow, UK

13 * Corresponding author. E-mail address: Cise.Unluer@glasgow.ac.uk

14
15 **Abstract**

16 This study investigated the healing efficiency and phase formations in pre-cracked
17 reactive magnesia-based binders under CO₂/water conditioning. Pre-loaded
18 samples with various crack widths were subjected to a healing regime involving
19 10% CO₂ and water for 10 cycles. The recovery of samples was assessed by
20 resonance frequency measurements and optical microscopy observations. A
21 relationship between crack width and type of healing phases was established via
22 microstructural analysis and carbonation depth measurements. All samples
23 achieved a complete stiffness recovery after a few healing cycles. The healed
24 cracks revealed a higher stiffness than the surrounding matrix under reloading.
25 The recovery of sample stiffness was associated with the densification of sample
26 microstructure via the formation of hydrated magnesium carbonates (HMCs).
27 Depending on the crack width and depth, two different types of HMCs
28 (nesquehonite and hydromagnesite) were observed within the healed cracks,
29 whose formation was influenced by pH, determined by the diffusion of CO₂.

30
31 **Keywords:** MgO; microcracking; self-healing; carbonation; microstructure

32 1. Introduction

33

34 Crack formation, which can occur at any stage during the life of a concrete
35 structure, can be caused by several external factors such as excessive loading
36 and shrinkage, resulting in detrimental effects on the performance and durability
37 of concrete structures [1, 2]. Traditional rehabilitation requires regular inspection
38 and maintenance, which is both labor and cost intensive. To alleviate these issues,
39 autogenous healing has been proposed for crack repair in concrete structures,
40 enabling the recovery of concrete performance without any human interference [1-
41 4]. Previous studies [5, 6] reported that the introduction of water conditioning
42 enabled the healing of cracks in cementitious materials, where the complete
43 healing of some cracks was shown. The widespread distribution of healing
44 compounds, including unhydrated cement particles, play a major role during the
45 autogenous healing of concrete. Present within the crack openings, these
46 compounds react with the water and CO₂ that penetrate from the natural
47 environment, leading to the subsequent formation of healing products that enable
48 crack closure [7].

49

50 Engineered Cementitious Composites (ECC) is a class of high performance fiber-
51 reinforced cementitious composites involving the use of a low dosage of synthetic
52 fibers (e.g. ≤ 2 vol.% polyvinyl alcohol fibers [8]) that is widely used to investigate
53 the self-healing behavior of concrete [9]. The crack opening of ECC can be
54 controlled at as low as 20 μm due to fiber bridging [10-12], demonstrating a good
55 self-healing potential under various environmental conditions. This is because
56 crack width greatly influences the self-healing performance of concrete, in which
57 narrower cracks heal more easily [1, 9].

58

59 Considering that the production of Portland cement (PC) is responsible for ~5-7%
60 of anthropogenic CO₂ emissions [13-15], there is a rising interest in the
61 development of concrete with reduced environmental impacts [16-18]. As a part of
62 the search for alternative materials with lower CO₂ emissions, reactive magnesia

63 cement (RMC) is being investigated due to its ability to gain strength via
64 carbonation and the lower temperatures (700-1000 °C) used during its production
65 in comparison with PC [19-21]. In addition to RMC systems, other magnesia-based
66 formulations that have been investigated and used in a number of construction
67 applications include magnesium oxychloride cements [22-24], magnesium
68 phosphate cements [25-31] and magnesium oxysulfate cements [32, 33].

69
70 The introduction of carbonation in the curing of RMC blends, which has been
71 widely studied [34-36], results in the formation of hydrated magnesium carbonates
72 (HMCs) via two major processes: (i) hydration of reactive MgO to form brucite
73 ($\text{Mg}(\text{OH})_2$) and (ii) reaction of brucite with CO_2 to form a series of HMCs. Some of
74 the major HMCs that have been identified within RMC-based mixes include
75 nesquehonite ($\text{Mg}(\text{HCO}_3)(\text{OH}) \cdot 2(\text{H}_2\text{O})$) and hydromagnesite
76 ($\text{Mg}_5(\text{CO}_3)_4(\text{OH})_2 \cdot 4(\text{H}_2\text{O})$). These HMCs have different morphologies, i.e.
77 hydromagnesite is identified via its rosette-like crystals [37, 38], whereas
78 nesquehonite has a needle-like morphology [39].

79
80 The feasibility of using RMC in ECC mixes was investigated in a previous study
81 [40], where an ultimate tensile strength and ductility of up to 3.7 MPa and 3.3%
82 were achieved, respectively. These values were comparable with normal PC-
83 based ECC. The evaluation of the environmental factors via the use of material
84 sustainability indicators also indicated that RMC-based ECC mixes could lead to a
85 reduction in the net CO_2 emissions of conventional ECC and concrete by 65% and
86 45% after 1 day of carbonation (i.e. under a CO_2 concentration of 99% and a
87 relative humidity of > 90% at room temperature), respectively [41]. Furthermore,
88 the low solubility of RMC leads to the presence of unreacted MgO particles within
89 the matrix [42-46], which is a desirable property for autogenous healing in
90 cementitious materials that requires the availability of reactive phases for the
91 healing of cracks [47]. Accordingly, the crack healing of RMC-based mixes
92 subjected to various healing regimes was investigated in recent studies [48-50],

93 where the formation of a large quantity of carbonate crystals enabled the complete
94 closure of cracks in RMC-based strain-hardening composites (SHC).

95

96 A number of investigations [5, 9] reported the importance of crack width in
97 influencing the self-healing capability of PC-based concrete. Yang et al. [5]
98 indicated that when crack width was larger than 150 μm , the resonance frequency,
99 which is used as a non-destructive indicator for the stiffness and crack healing
100 recovery of concrete structures, was greatly reduced and could not be regained
101 even under water curing. These outcomes revealed the difficulty of repairing large
102 crack openings in ECC samples. Similarly, within ECC samples containing slag,
103 cracks of up to 100 μm could be completely sealed after a period of 60 days when
104 subjected to water-air regime [51]. Another study [9] indicated that the inclusion of
105 up to 30% slag led to the complete healing of cracks with an opening of 80-90 μm .
106 Regarding the healing products, a number of studies [1, 52] indicated that the
107 formation of calcium carbonate via the reaction between atmospheric CO_2 and Ca-
108 bearing phases enabled the closure of cracks in PC-based samples. In slag-rich
109 samples, a mixture of CaCO_3 and C-S-H was identified as the major healing
110 product [9].

111

112 Although the influence of crack width on the self-healing efficiency of PC-based
113 mixes has been thoroughly investigated, previous studies [48, 53] indicated that a
114 different scenario was seen in RMC-based systems due to the presence of
115 different healing products (i.e. hydrated magnesium carbonates) with varying
116 morphologies. These variations affected the final performance of the samples, in
117 which the relationship between the tensile strength (strain) recovery and crack
118 width was not consistent. In this respect, the pH and the carbon content in the local
119 environment within the cracks may influence the types of healing phases that form.
120 Accordingly, the formation of different phases with varying properties and
121 morphologies were thought to play an important role in the self-healing efficiency
122 of RMC-based binders. Considering that magnesia has been widely used as an
123 expansive agent in cementitious materials due to its delayed hydration, which

124 compensates for the thermal shrinkage of concrete structures (e.g. dams) [54], if
125 the role of crack width on the self-healing efficiency of RMC-based binders was
126 fully understood, it could provide some guidance in terms of crack control actions
127 and measures in concrete structures containing magnesia.

128

129 Building on the existing knowledge on the self-healing mechanism of RMC-based
130 SHC [53, 55], this study focused on the crack healing efficiency and phase
131 formations within different cracks observed in RMC-based SHC. As the CO₂
132 concentration in ambient air is low (i.e. ~0.04%), in order to be able to obtain results
133 within a reasonable time frame for a scientific study, the CO₂ concentration used
134 in this study was elevated to simulate the self-healing of RMC-based samples,
135 albeit at an accelerated rate. Previous studies [34, 56] have shown that RMC-
136 based mixes can also carbonate under ambient conditions, therefore resulting in
137 a similar finding in a longer duration. Therefore, to prepare the samples for self-
138 healing, they were initially pre-loaded to create a number of single crack widths,
139 followed by subjecting to 10% CO₂ and water conditioning for 10 cycles (i.e. a total
140 of 20 days), based on previous studies [48, 53]. The healing efficiency of the
141 initially marked cracks was evaluated via resonance frequency measurement and
142 optical microscope observation. After the assessment of healing efficiency, the
143 healed samples were re-loaded to analyze subsequent performance and crack
144 formation. Differing from existing studies, this paper is the first in the literature to
145 explore the relationship between crack width and types and properties of healing
146 products that form within each crack. This was facilitated through a systematic and
147 comprehensive investigation of several cracks, whose widths were manually
148 adjusted via the clamping of two polished pieces of RMC-based samples. Scanning
149 electron microscopy (SEM), energy-dispersive x-ray (EDX)
150 spectroscopy and carbonation depth measurements were used to analyze the
151 types and properties of healing products in different crack widths.

152

153

154 **2. Materials and Methodology**

155

156 **2.1. Materials and sample preparation**

157

158 The main binder used in the prepared samples, RMC, was obtained from
159 International Scientific Ltd. (Singapore). Class F fly ash (FA), supplied by Bisley
160 Asia Ltd. (Malaysia), was used to adjust the rheology of the prepared mixes for
161 desirable fiber dispersion, in line with the findings of previous studies [40]. The
162 chemical composition and particle size distribution of RMC (SSA: 16.3 g/m²) and
163 FA are shown in Table 1 and Fig. 1, respectively. The median particle size (d₅₀) of
164 RMC and FA was recorded as 13.7 μm and 2.5 μm, respectively. Polyvinyl alcohol
165 (PVA) fibers were obtained from Kuraray Ltd. (Japan). The morphology of PVA
166 fibers is shown in Fig. 2, whereas their physical properties are listed in Table 2.
167 Sodium hexametaphosphate (Na(PO₃)₆), supplied by VWR International Ltd.
168 (Singapore), was used as a water reducer in the prepared mixes [40].

169

170 Table 3 shows the mix design proportions of RMC-based SHC samples prepared
171 in this study. A relatively low fiber dosage (i.e. 0.5% by volume) was included to
172 prevent multiple cracking and to allow the formation of a single crack upon pre-
173 loading for the investigation of the effect of crack width on self-healing [57]. To
174 prepare the fresh mixtures, RMC and FA were first dry mixed for over 2 minutes,
175 after which the water containing Na(PO₃)₆ was slowly added into the mixture. After
176 another 2-3 minutes of mixing (i.e. until a homogenous mixture was achieved), the
177 PVA fibers were slowly placed into the mixer within 2 minutes. The prepared
178 mixture was cast into dog-bone shaped molds (Fig. 3(a)) for pre-loading, to obtain
179 different single crack widths before autogenous healing. For the investigation of
180 the influence of crack width on the types and properties of healing products, the
181 same mix design proportions shown in Table 3 were used by excluding fibers. The
182 prepared pastes were cast into 50x50x50 mm cubic molds. Before demolding, the
183 cast dog-bone and cubic samples were stored in a sealed container for 3 days,
184 accompanied with silica gel for dehumidification. These samples were then

185 demolded and cured in an incubator under 10% CO₂, 30°C and 90% relative
186 humidity (RH) for 7 days to enable strength gain.

187

188 Once their curing was completed, the dog-bone samples were removed from the
189 incubator and subjected to pre-loading under uniaxial tension at a loading rate of
190 0.5 mm/min to obtain different single crack widths (Fig. 3(b)). All the cracks were
191 clearly marked before conditioning. The cracked samples were submerged into
192 water for 24 hours, followed by curing under 10% CO₂, 30°C and 90% RH in an
193 incubator for another 24 hours. In addition to CO₂ concentration, temperature and
194 relative humidity would also affect the healing process as the reaction mechanisms
195 (i.e. hydration and carbonation) of reactive magnesia is dependent on these
196 parameters. Therefore, the CO₂ concentration, temperature and relative humidity
197 were kept constant in this study to avoid any variations on the final outcomes.

198

199 The findings revealed in previous studies [53] indicated that the crack width
200 obtained under different pre-strain levels influenced the healing efficiency of RMC-
201 based binders. This outcome was reflected by a series of indicators such as tensile
202 strength and resonance frequency recovery. The types and properties of healing
203 phases formed within the cracks also played an important role in the healing
204 efficiency of samples. Therefore, to evaluate the relationship between crack width
205 and types/properties of healing products, a systematic and comprehensive study
206 involving the use of samples with various crack widths was performed. As the
207 internal parts of RMC-based samples were not fully carbonated [58], they
208 presented a potential for further carbonation and self-healing. Accordingly, the
209 prepared cubic samples were cut into 20x20x20 mm pieces by a diamond saw.
210 Two pieces from each sample were thoroughly polished by sandpaper and
211 clamped together by facing each other via the use of G-clamps for the creation of
212 different crack widths with dimensions of < 50 μm, 50-100 μm, 100-150 μm and >
213 200 μm, with the assistance of an optical microscope.

214

215 2 samples with 4 surfaces containing healing phases were prepared and
216 investigated for each crack width to increase the repeatability of this assessment.
217 The crack widths were related with the various roughness of fracture surfaces and
218 were controlled via the variation of the polishing duration and the pressure used
219 during the clamping of samples. In this respect, samples that were polished for a
220 longer time and clamped using a higher pressure presented smaller crack widths
221 due to the smoother fracture surfaces. The flow chart revealing the steps involved
222 in this preparation process is shown in Fig. 4. These samples that were prepared
223 for the assessment of different crack widths were subjected to the same healing
224 regimes as the pre-cracked dog-bone samples. When the healing process was
225 completed, the samples were released from the G-clamps to expose the healing
226 products that formed in-between the two surfaces. Microstructural analysis and
227 carbonation depth measurements were then performed on these exposed sections.
228 The representation of the healing process and the exposure of the final healing
229 products for further analysis are shown in Fig. 5.

230

231

232 **2.2. Methodology**

233

234 Transverse resonant frequency (RF) of the prepared samples was measured
235 before, during and after the healing process, which served as an indirect and
236 simple approach to evaluate the healing efficiency by observing the stiffness
237 recovery after healing. RF was measured according to ASTM C215 [59], with a
238 span of 200 mm between the roller supports. The average RF of each sample was
239 obtained from 10 separate measurements.

240

241 The crack widths in each sample were observed under an OPTEM Zoom 70XL
242 microscope. The images were captured by a Nikon DS-Fi2 high resolution camera
243 equipped with NIS Elements (Nikon) software, at a magnification of 420×.

244

245 The loading of the samples before and after healing was conducted under uniaxial
246 tension at a rate of 0.5 mm/min by using the test setup shown in Fig. 3(b).

247

248 Prior to SEM-EDX analysis, the exposed sections were coated with platinum under
249 a current of 30 mA for 30 seconds. The coated samples were then investigated via
250 a field emission scanning electron microscope (JOEL JSM-7600F) and energy-
251 dispersive X-ray spectroscopy (Oxford X-max 80 mm²).

252

253 A phenolphthalein pH indicator was sprayed on the cleaned surface of each
254 sample to assess the carbonation depth. The indicator used was a phenolphthalein
255 1% ethanol solution with 1 g phenolphthalein and 90 ml 95.0 V/V% ethanol diluted
256 in 100 ml water [60]. When the indicator was applied on sample surfaces, a change
257 in the color to pink indicated the presence of OH⁻ ions, (i.e. pH value of > 10),
258 whereas a lack of change in the color reflected the lower presence of OH⁻ ions (i.e.
259 pH < 8.2), providing a general idea about the progress of carbonation at different
260 depths of the prepared samples [61]. Due to its ease of application, several studies
261 [41, 62, 63] measured the carbonation depth of RMC-based binders via the use of
262 phenolphthalein pH indicator, although its accuracy is questionable. In this study,
263 after the completion of the healing process, the clamped samples were re-opened
264 and their surfaces were sprayed with phenolphthalein pH indicator. To increase
265 the accuracy of this test, the average depth of the colorless phenolphthalein region
266 was measured from four different points located perpendicularly to the four edges
267 on each cross section. The samples were left for 24 hours prior to these
268 measurements. An OPTEM Zoom 70XL optical microscope was also employed to
269 measure the carbonation depth. The images were obtained using a Nikon DS-Fi2
270 high resolution camera equipped with NIS Elements (Nikon) software at a
271 magnification of 420×. The measurement process of carbonation depth is
272 illustrated in Fig. 6. To prove the repeatability of the performed tests, the findings
273 generated through this testing could also be indirectly confirmed by our [48, 53]
274 and other researchers' [49] studies.

275

276

277 **3. Results**

278

279 Pre-loaded samples with various crack widths were prepared, as shown in Fig. 3.
280 The self-healing process within the samples was investigated via the measurement
281 of resonance frequency, optical microscope observations and following a re-
282 loading procedure, whose details are included in Sections 3.1-3.3.

283

284

285 **3.1. Assessment of crack healing via resonance frequency (RF)** 286 **measurements**

287

288 Serving as a non-destructive method, RF ratios (i.e. normalized with respect to the
289 original/unloaded samples), listed in Table 4, were used to evaluate the stiffness
290 and healing recovery of samples subjected to CO₂/water conditioning at every two
291 cycles. The single crack width of samples ranged from 23.4 to 120.8 μm, which
292 met the requirements of this study. Depending on the crack width, the RF ratios
293 indicated a drop of various degrees due to the reduction in the stiffness of samples
294 linked with the formation of the cracks. As can be seen, crack width had a direct
295 influence on the RF ratios, generally leading to a more obvious decline in RF as
296 the crack width increased. As healing proceeded, the pre-cracked samples
297 revealed a rapid increase in the RF ratio over time due to the formation of healing
298 products, enabling the healing of cracks and recovery of stiffness. After the
299 completion of the healing process, nearly all the samples revealed > 100% RF
300 ratios, indicating a complete recovery of stiffness within the scope of crack width
301 investigated. While a steady increase in the RF ratios was observed during the first
302 cycle of healing (i.e. from RF₀ to RF₂), the rate of RF increase gradually slowed
303 down and ceased after a few cycles, demonstrating the limited benefits of
304 excessive CO₂ exposure in the improvement of sample stiffness over time. The
305 results clearly showed that CO₂ conditioning was very effective in enabling the self-
306 healing of RMC-based SHC as some samples revealed a complete recovery of

307 stiffness after only 2 cycles, indicating that self-healing occurred within a short
308 period of time under CO₂/water conditioning. This recovery was attributed to the
309 rapid formation of healing phases due to the high concentration of CO₂ (i.e. 10%)
310 used in this study. According to these findings, the healing period could be
311 shortened to less than 10 cycles to achieve a similar efficiency, leading to complete
312 crack healing.

313

314 In addition to the phases that formed within the cracks during the healing process,
315 the RF ratios may also be influenced by the continuation of hydration and
316 carbonation within the sample matrix. In order to investigate the influence of this
317 factor, a set of control samples was cast with the same mix design shown in Table
318 3. Without pre-cracking, these samples were subjected to the same healing regime
319 as the pre-cracked samples. The revised RF ratios normalized with respect to the
320 control samples are shown in Fig. 7. The figure indicated that the revised RF ratios
321 also reduced with increasing crack width. The increase of RF ratios due to the
322 hydration or carbonation of samples was negligible, revealing that the recovery of
323 RF ratio was mainly attributed to the formation of phases within the cracks during
324 the healing process as the hydration and carbonation reactions within the sample
325 matrix only played a minor role in the recovery of the RF ratios.

326

327

328 **3.2. Progress of healing observed via optical microscopy**

329

330 Fig. 8 shows the progress of crack healing within samples with various crack
331 openings under the CO₂/water regime they were subjected to for up to 10 cycles.
332 These images indicated that two types of crack healing occurred among these
333 samples, identified as (i) internal healing (i.e. at crack widths > 100 μm) and (ii)
334 mixed healing (i.e. at crack widths < 100 μm).

335

336 The “internal healing” of cracks usually took place when the crack width was
337 greater than 100 μm. In this scenario, the healing products initially formed at the

338 inner sections of the cracks, accompanied with a small amount of precipitation on
339 the surfaces or the edges of the cracks, as seen in Fig. 8(a). The adequate crack
340 widths within these samples allowed the diffusion of CO₂ into the interior sections
341 of the cracks, without sealing the top layer at early stages. Another type of healing
342 identified as “mixed healing” took place in samples with crack widths of < 100 μm.
343 This process involved a combination of surface and internal healing as healing
344 products were observed both at the edges and inner sections of the cracks, as
345 shown in Fig. 8(b). Accordingly, the healing products started to grow on the top
346 layer and inner sections of the cracks simultaneously. As healing progressed, the
347 top layer of the crack was eventually sealed as the crack opening was not too wide,
348 meanwhile also enabling the filling of the internal regions of the cracks with healing
349 products. This combined mechanism defined “mixed healing” as a more favorable
350 form of healing in RMC samples due to the higher healing efficiency achieved
351 when compared to “internal healing”. This was in line with the results shown in Fig.
352 7, where samples with smaller crack widths achieved greater RF ratios due to their
353 better healing performance.

354

355 This difference in the healing pattern could be attributed to the difficulty in covering
356 the top layer of the cracks with larger widths in samples undergoing “internal
357 healing”, although the healing products still formed around the edges. This led to
358 the precipitation of the healing products only at the inner sections of the cracks.
359 Nevertheless, longer durations may be needed for the formation of healing phases
360 and stiffness recovery in samples containing MgO with a lower reactivity.

361

362

363 **3.3. Crack formation after reloading**

364

365 Selected samples were subjected to reloading after the completion of the healing
366 process, by following the same procedure performed earlier in pre-loading. The
367 results of this reloading process, shown in Fig. 9, revealed the formation of new
368 cracks at different locations than those of the original/healed cracks in samples

369 that experienced “mixed healing”. This outcome suggested that the binding
370 strength of the products that formed during the healing process was relatively high,
371 resulting in a similar or even higher stiffness when compared with the rest of the
372 sample matrix. This finding was in line with the RF results shown in Section 3.1,
373 where $\geq 100\%$ RF ratios were recovered in pre-cracked samples after 10 cycles of
374 healing. A similar outcome was reported in earlier studies [64], where the
375 investigation of the influence of self-healing on the fatigue performance of SHC
376 indicated the role of self-healing in not only healing the cracks within the matrix,
377 but also recovering the fiber/matrix interfacial bond due to an increase in the
378 frictional bond. This improvement could be attributed to the microstructural
379 changes at the interface (i.e. the debonded fiber/matrix interface was enhanced
380 through the formation of hydrate and/or carbonate phases during self-healing) [64].
381 The overall results indicated that the improved fiber/matrix bonding at the healed
382 cracks led to the formation of new cracks at different locations instead of the
383 original ones [64].

384

385

386 **4. Further Explanations and Discussion**

387

388 In the pre-loaded samples with various crack widths, the phases that formed during
389 the healing process revealed different morphologies at different crack widths, when
390 observed closely (Fig. 10). This variation in the morphology of carbonate crystals
391 was an indication of the formation of different types of healing products within the
392 cracks, highlighting that the crack width may play a major role in determining the
393 properties of the formed phases. Therefore, to elucidate the relationship between
394 crack width and type of phases that formed as a result of the healing process,
395 samples with different crack widths were manually prepared by following the
396 procedure outlined in Figs. 4 and 5. The healing products observed in each sample
397 with different crack widths were studied closely via microstructural analysis
398 (Section 4.1), while the carbonation depths of samples with various crack widths
399 were also measured to explain the variations in healing products along the sample

400 depth (Section 4.2). The relationship between the self-healing behavior, stiffness
401 (strength) recovery and crack width (depth) of RMC-based samples was also
402 clarified based on relevant previous experimental outcomes and data presented in
403 the literature [48, 53] (Section 4.3). Finally, a model explaining the variation in
404 healing products observed in RMC-based samples was also proposed to present
405 a detailed analysis (Section 4.4).

406

407

408 **4.1. Formation of phases at different crack widths in RMC-based samples**

409

410 A clarification of the relationship between different crack widths and types of
411 healing products was performed via the use of SEM-EDX, for which samples with
412 4 ranges of crack widths (i.e. $< 50 \mu\text{m}$, $50\text{-}100 \mu\text{m}$, $100\text{-}150 \mu\text{m}$ and $> 200 \mu\text{m}$)
413 were generated according to the procedure outlined in Fig. 4. After the completion
414 of 10 cycles of healing under CO_2 /water conditioning, the newly formed phases
415 within each crack were analyzed through microstructural analysis (Fig. 11). Fig.
416 11(a)-(d) shows the microstructural images of the healing products that formed at
417 the edges and inner sections of cracks with different widths. When the crack width
418 was $< 50 \mu\text{m}$, the formation of HMC crystals with different morphologies were
419 observed, whose type depended on the location of healing. Accordingly, the
420 morphologies of the healing products observed at the edges (i.e. section ranging
421 from the top surface to a depth of $\sim 1 \text{ mm}$) of cracks varied from those observed at
422 the inner sections (Fig. 11(a)). The morphologies of crystals formed at the edges
423 of cracks hinted the formation of needle-like nesquehonite (Fig. 11(a1)), whereas
424 those forming around the inner sections revealed the formation of rosette-like
425 hydromagnesite (Fig. 11(a2)) [37, 39, 42, 65]. The elemental mapping of these two
426 types of crystals, presented in Fig. 12(a) and (b), illustrated the presence of Mg, O
427 and C, confirming that these healing products observed after 10 cycles of healing
428 under CO_2 /water conditioning were HMC phases.

429

430 In the case of crack widths ranging between 50 and 100 μm , a similar distribution
431 of healing products as those presented earlier in Fig. 11(a) was observed. The
432 variation in the morphologies of the formed HMCs was also similar, where
433 nesquehonite was observed at the edges (Fig. 11(b1)) and hydromagnesite
434 dominated the inner sections (Fig. 11(b2)). When the crack width increased to 100-
435 150 μm (Fig. 11(c)), nesquehonite was still the major healing product at crack
436 edges (Fig. 11(c1)). However, a different scenario was revealed at the inner
437 sections of these cracks (Fig. 11(c2)-(c4)), where a combination of
438 hydromagnesite and nesquehonite was identified, indicating that these two types
439 of HMCs were intermixed with each other at greater crack widths (100-150 μm).
440 When the crack width was further extended to $> 200 \mu\text{m}$, a different outcome was
441 observed, where nesquehonite prevailed both at the edges (Fig. 11(d1)) and inner
442 sections (Fig. 11(d2)) of the cracks.

443

444

445 **4.2. Assessment of carbonation depth in RMC-based samples**

446

447 Fig. 13 shows the carbonation depth of samples with various crack widths
448 calculated according to the equation shown in Fig. 6. The carbonation depth
449 generally increased with the growth of crack width, hinting a higher extent of
450 carbonation and a lower pH. This increase in carbonation depth was attributed to
451 the accessibility of the sample matrix in the interior regions of the cracks to CO_2
452 and water as the crack opening was larger. At these larger widths, a wider diffusion
453 channel was provided for the ingress of CO_2 and water, enabling a further degree
454 of reaction with the surrounding cement matrix. An increase in the pH values and
455 an associated reduction in the degree of carbonation was observed at greater
456 crack depths, which was an indication of the limited CO_2 diffusion as crack depth
457 increased. This was because while the top layers and the edges of the cracks were
458 directly exposed to high concentrations of CO_2 , resulting in a greater extent of
459 carbonation and a lower pH; it took a longer time for CO_2 and water to access the
460 inner regions of the cracks. Earlier studies [66] also reported the direct relationship

461 with carbonation depth and time, explaining the changes observed in the
462 carbonation degree and hence pH of the prepared samples. Furthermore, the rapid
463 formation of HMCs on the outer edges and top layers of the cracks led to the
464 sealing of crack surfaces under a high CO₂ concentration, which was also
465 observed in previous studies [36]. This resulted in the isolation of the inner regions
466 from further access to CO₂ and water, increasing the time it took for carbonation to
467 take place at the inner sections of the cracks.

468

469

470 **4.3. Relationships among the self-healing behaviors, stiffness (strength)** 471 **recovery and crack width (depth) in RMC-based samples**

472

473 Previous research [56, 67] has shown that RMC samples subjected to accelerated
474 CO₂ curing similar to the conditions presented in this paper still contained large
475 amounts of uncarbonated MgO and brucite (Mg(OH)₂) even after 28 days of curing.
476 This led to a large amount of Mg²⁺ ions remaining within the sample matrix, which
477 is a prerequisite for healing. Accordingly, when the RMC-based SHC samples
478 prepared in this study were subjected to CO₂/water conditioning, the original solid
479 phases within the cracks acted as preferential locations for heterogeneous
480 nucleation (i.e. the seeding of the nuclei of new phases into the original/existing
481 phases) [68]. During the healing process, the reaction of leached Mg²⁺ ions with
482 the dissolved CO₂ in the presence of water on the surface of the crack led to the
483 initial deposition of HMCs (i.e. nesquehonite) once the ion concentrations on the
484 surface/outer edges of the cracks reached the saturation point. The formation of
485 these phases acted as nucleation sites for the subsequent precipitation of
486 carbonates, enabling the rapid sealing of the top layer of the cracks via the
487 formation of healing products, as reported earlier in [48]. Similarly, the internal
488 sections of the cracks underwent healing, during which the precipitation of HMCs
489 such as nesquehonite, hydromagnesite or a mixture of both, was observed. The
490 formation of these phases at the internal sections initially started when the
491 saturation point was reached due to a rise in the ion concentrations, followed by

492 further precipitations on the existing phases that acted as nucleation seeds for the
493 formation of new carbonate phases, enabling the internal healing of the cracks.
494 Closer observations of the phase formations revealed that the degree of healing
495 as well as the type of phases that formed within each crack directly depended on
496 the crack widths.

497

498 The rapid recovery of RF after only a few healing cycles was attributed to the
499 formation of elongated nesquehonite needles on the top surfaces and the outer
500 edges of the cracks. Accordingly, the formation of nesquehonite enabled the
501 densification of the sample microstructure, thereby increasing the overall stiffness
502 of RMC samples. This was because the conversion of the main hydrate phase in
503 RMC systems, brucite (i.e. density of 2.37 g/cm^3) [69], into nesquehonite (i.e.
504 density of 1.85 g/cm^3) [70] resulted in an expansion of the solid volume by a factor
505 of ~ 2.3 . This outcome was in line with the findings of previous studies [71], where
506 the enhancement of the stiffness of RMC-based samples subjected to accelerated
507 CO_2 curing was reported. Furthermore, the formation of needle-like nesquehonite
508 was proven to have a higher contribution to strength and stiffness than rounded or
509 tabular crystals due to its 3D structure [36].

510

511 The stiffness recovery of samples is highly related with the success of self-healing
512 of cracks, whose width and depth also play an important role in the self-healing
513 efficiency (i.e. reflected by the volume of healing phases that form within the crack).
514 Previous studies [72] reported that the self-healing efficiency of PC systems
515 subjected to water/air cycles significantly relied on the crack depth. Within these
516 samples, precipitation of phases took place rapidly near the top surface of the
517 crack, which inhibited the further formation of phases at greater depths, leading to
518 a non-uniform self-healing pattern throughout the crack depth. A similar outcome
519 was reported in RMC-based systems subjected to wetting and drying cycles, in
520 which the healing efficiency was reduced and dominated by the lower densities of
521 healing products at the inner sections [49]. Alternatively, when subjected to

522 bacterial conditioning, RMC samples revealed a ~78% increase in the amount of
523 crystals that formed at the top surface of cracks when compared to the bottom [48].

524

525 In terms of strength and strain recovery, RMC-based samples with smaller cracks
526 presented a similar tensile strength recovery than their counterparts containing
527 larger cracks after 10 cycles of water/CO₂ curing healing [53]. On the other hand,
528 samples with larger cracks revealed a better performance than those with smaller
529 cracks in strain recovery. After 10 cycles of healing, all the pre-cracked samples
530 outperformed those that were not subjected to any pre-loading with regards to their
531 final tensile strength and strain. These results were associated with the formation
532 of hydrate/carbonate crystals that formed between the fiber and the matrix,
533 enhancing their bond and overall mechanical performance [64].

534

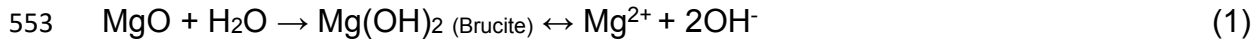
535

536 **4.4. A model explaining the healing phase variations in RMC-based samples**

537

538 Another factor that is known to influence the precipitation of HMCs is pH [73, 74].
539 Since the bicarbonate ion (HCO₃⁻) prevails instead of CO₃²⁻ in low pH environments,
540 the nucleation rate of Mg²⁺ and CO₃²⁻ was greatly restricted as CO₃²⁻ ions generally
541 existed in the form of HCO₃⁻ [74]. Previous studies [75] reported the presence of
542 HCO₃⁻ and OH⁻ bands when nesquehonite was analyzed under Raman
543 spectroscopy. In the case of internal healing, when compared to cracks with small
544 widths, the relatively larger cracks (> 200 μm) resulted in a higher extent of
545 carbonation and lower pH due to the broader transport path provided for the
546 diffusion of CO₂. This facilitated the abundant formation of HCO₃⁻ ions that favored
547 the precipitation of nesquehonite (Mg(HCO₃)(OH)·2H₂O), as shown in Equations
548 1-3. This mechanism was also valid for the healing of the crack surfaces and outer
549 edges, where nesquehonite was identified as the main HMC phase that formed
550 during the healing process due to the widespread presence of HCO₃⁻ in the low pH
551 environment enabled by the continuous diffusion of CO₂.

552



554



556



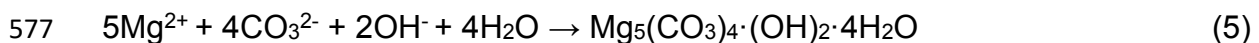
558

559 Alternatively, when the crack width was relatively small ($< 50 \mu m$), CO_3^{2-} ions
560 became dominant in the inner sections of these cracks as compared to HCO_3^- ions,
561 due to the increase in pH. The high pH values were associated with the low
562 carbonation degrees caused by the limited diffusion of CO_2 within these smaller
563 crack widths, favoring the formation of hydromagnesite ($Mg_5(CO_3)_4(OH)_2 \cdot 4H_2O$)
564 (Equations 1, 4 and 5) as opposed to nesquehonite in the interior sections. As
565 expected, a “transitional” crack width, where the concurrent formation of
566 nesquehonite and hydromagnesite was observed due to the co-existence of CO_3^{2-}
567 and HCO_3^- within the cracks, could be identified. The conversion of
568 hydromagnesite into nesquehonite with a further reduction in the pH of the solution,
569 as reported earlier [48], could also result in the formation of a mixture of
570 nesquehonite and hydromagnesite. The relationship between the formation of
571 different types of HMCs and crack width as well as depths was revealed in Fig. 14,
572 highlighting the variation in phase formations with respect to the physical
573 properties of the cracks.

574



576



578

579

580 **5. Conclusions**

581

582 The results of this study have indicated the effective use of CO_2 /water conditioning
583 in the healing of cracks within reactive magnesia cement (RMC) based binders via

584 the production of hydrated magnesium carbonates (HMCs). Introduction of a high
585 concentration (10%) of CO₂ enabled the rapid healing of cracks and improved the
586 overall stiffness of pre-cracked samples within a short period of time. The healed
587 cracks revealed a higher stiffness than the surrounding matrix under reloading,
588 which resulted in the formation of new cracks. The recovery of sample stiffness
589 was associated with the densification of sample microstructure via the formation
590 of HMCs. Depending on the crack width, the initial precipitation of these carbonate
591 phases led to the sealing of the crack surfaces, creating a barrier for the continuous
592 diffusion of CO₂ and water into the inner sections of the cracks.

593

594 The major healing products within the cracks of the RMC-based SHC samples
595 subjected to CO₂/water conditioning were recognized as two commonly observed
596 HMCs, namely nesquehonite and hydromagnesite. The formation of these phases
597 relied on the pH within the cracks, which was influenced by the physical properties
598 (i.e. width and depth) of the cracks. Nesquehonite was the main phase observed
599 in cracks with large widths and at the edges of all cracks, independent of their
600 width, due to the low pH environment enabled by the continuous access to CO₂
601 within these regions. Alternatively, hydromagnesite was identified as the main
602 carbonate phase in the internal sections of cracks with smaller widths due the
603 lower degree of carbonation (i.e. higher pH) within these regions. The analysis of
604 different crack widths revealed a transitional crack width where the concurrent
605 formation of nesquehonite and hydromagnesite was observed.

606

607 Overall, the findings presented in this study clearly highlighted that the progress of
608 the healing process within RMC-based SHC samples is highly dependent on the
609 crack width and depth, which influence the degree of carbonation and the type of
610 final phases that control the mechanical performance. Further studies will look into
611 the effect of the binder components by evaluating the influence of their chemical
612 and physical properties on the self-healing efficiency of RMC-based samples.

613

614

615 **Acknowledgement**

616

617 The authors would like to acknowledge the financial support from the Singapore
618 MOE Academic Research Fund Tier 1 (RG 95/16) and Singapore MOE Academic
619 Research Fund Tier 2 (MOE2017-T2-1-087 (S)) for the completion of this research
620 project.

References

- [1] H.-W. Reinhardt, M. Jooss, Permeability and self-healing of cracked concrete as a function of temperature and crack width, *Cement and Concrete Research* 33(7) (2003) 981-985.
- [2] S. Granger, A. Loukili, G. Pijaudier-Cabot, G. Chanvillard, Experimental characterization of the self-healing of cracks in an ultra high performance cementitious material: Mechanical tests and acoustic emission analysis, *Cement and Concrete Research* 37(4) (2007) 519-527.
- [3] C. Clear, The effects of autogenous healing upon the leakage of water through cracks in concrete, Cement and Concrete Association, Wexham Spring, May (1985).
- [4] S. Jacobsen, J. Marchand, H. Hornain, SEM observations of the microstructure of frost deteriorated and self-healed concretes, *Cement and Concrete Research* 25(8) (1995) 1781-1790.
- [5] Y. Yang, M.D. Lepech, E.-H. Yang, V.C. Li, Autogenous healing of engineered cementitious composites under wet-dry cycles, *Cement and Concrete Research* 39(5) (2009) 382-390.
- [6] Y. Yang, E.-H. Yang, V.C. Li, Autogenous healing of engineered cementitious composites at early age, *Cement and Concrete Research* 41(2) (2011) 176-183.
- [7] J. Cowie, F. Glasser, The reaction between cement and natural waters containing dissolved carbon dioxide, *Advances in Cement Research* 4(15) (1992) 119-134.
- [8] V.C. Li, On engineered cementitious composites (ECC), *Journal of Advanced Concrete Technology* 1(3) (2003) 215-230.
- [9] J. Qiu, H.S. Tan, E.-H. Yang, Coupled effects of crack width, slag content, and conditioning alkalinity on autogenous healing of engineered cementitious composites, *Cement and Concrete Composites* 73 (2016) 203-212.
- [10] E.-H. Yang, Y. Yang, V.C. Li, Use of high volumes of fly ash to improve ECC mechanical properties and material greenness, *ACI Materials Journal* 104(6) (2007) 620-628.

- [11] D. Zhang, J. Yu, H. Wu, B. Jaworska, B.R. Ellis, V.C. Li, Discontinuous micro-fibers as intrinsic reinforcement for ductile Engineered Cementitious Composites (ECC), *Composites Part B: Engineering* (2020) 107741.
- [12] H.-L. Wu, J. Yu, D. Zhang, J.-X. Zheng, V.C. Li, Effect of morphological parameters of natural sand on mechanical properties of engineered cementitious composites, *Cement and Concrete Composites* 100 (2019) 108-119.
- [13] E. Benhelal, G. Zahedi, E. Shamsaei, A. Bahadori, Global strategies and potentials to curb CO₂ emissions in cement industry, *Journal of Cleaner Production* 51 (2013) 142-161.
- [14] L.K. Turner, F.G. Collins, Carbon dioxide equivalent (CO₂-e) emissions: A comparison between geopolymer and OPC cement concrete, *Construction and Building Materials* 43 (2013) 125-130.
- [15] C. Ma, G. Long, Y. Shi, Y. Xie, Preparation of cleaner one-part geopolymer by investigating different types of commercial sodium metasilicate in China, *Journal of Cleaner Production* 201 (2018) 636-647.
- [16] G. Kastiukas, S. Ruan, S. Liang, X. Zhou, Development of precast geopolymer concrete via oven and microwave radiation curing with an environmental assessment, *Journal of Cleaner Production* (2020) 120290.
- [17] B. Panda, S. Ruan, C. Unluer, M.J. Tan, Investigation of the properties of alkali-activated slag mixes involving the use of nanoclay and nucleation seeds for 3D printing, *Composites Part B: Engineering* (2020) 107826.
- [18] S. Ruan, C. Unluer, Influence of supplementary cementitious materials on the performance and environmental impacts of reactive magnesia cement concrete, *Journal of Cleaner Production* 159 (2017) 62-73.
- [19] L. Vandeperre, M. Liska, A. Al-Tabbaa, Microstructures of reactive magnesia cement blends, *Cement and Concrete Composites* 30(8) (2008) 706-714.
- [20] M. Liska, A. Al-Tabbaa, Ultra-green construction: reactive magnesia masonry products, *Proceedings of ICE-Waste and Resource Management* 162(4) (2009) 185-196.
- [21] S. Ruan, C. Unluer, Comparative life cycle assessment of reactive MgO and Portland cement production, *Journal of Cleaner Production* 137 (2016) 258-273.

- [22] G. Kastiukas, S. Ruan, C. Unluer, S. Liang, X. Zhou, Environmental assessment of magnesium oxychloride cement samples: A case study in Europe, *Sustainability* 11(24) (2019) 6957.
- [23] P. He, C.S. Poon, D.C. Tsang, Using incinerated sewage sludge ash to improve the water resistance of magnesium oxychloride cement (MOC), *Construction and Building Materials* 147 (2017) 519-524.
- [24] P. He, M.U. Hossain, C.S. Poon, D.C. Tsang, Mechanical, durability and environmental aspects of magnesium oxychloride cement boards incorporating waste wood, *Journal of Cleaner Production* 207 (2019) 391-399.
- [25] L. Wang, K. Iris, D.C. Tsang, K. Yu, S. Li, C.S. Poon, J.-G. Dai, Upcycling wood waste into fibre-reinforced magnesium phosphate cement particleboards, *Construction and Building Materials* 159 (2018) 54-63.
- [26] L. Wang, K. Iris, D.C. Tsang, S. Li, J.-s. Li, C.S. Poon, Y.-S. Wang, J.-G. Dai, Transforming wood waste into water-resistant magnesia-phosphate cement particleboard modified by alumina and red mud, *Journal of cleaner production* 168 (2017) 452-462.
- [27] Y. Weng, S. Ruan, M. Li, L. Mo, C. Unluer, M.J. Tan, S. Qian, Feasibility study on sustainable magnesium potassium phosphate cement paste for 3D printing, *Construction and Building Materials* 221 (2019) 595-603.
- [28] C. Ma, B. Chen, Properties of magnesium phosphate cement containing redispersible polymer powder, *Construction and Building Materials* 113 (2016) 255-263.
- [29] C. Ma, B. Chen, Experimental study on the preparation and properties of a novel foamed concrete based on magnesium phosphate cement, *Construction and Building Materials* 137 (2017) 160-168.
- [30] G. Yi, C. Ma, G. Long, B. Zhao, Y. Xie, Effects of metakaolin on a novel aerated magnesium phosphate cement with high early strength, *Construction and Building Materials* 187 (2018) 1130-1133.
- [31] Y. Li, G. Zhang, Z. Wang, Experimental-computational approach to investigate nanoindentation of magnesium potassium phosphate hexahydrate (MKP) with X-CT technique and finite element analysis, *Frontiers in Materials* 6 (2019) 344.

- [32] C. Wu, H. Yu, H. Zhang, J. Dong, J. Wen, Y. Tan, Effects of phosphoric acid and phosphates on magnesium oxysulfate cement, *Materials and Structures* 48(4) (2015) 907-917.
- [33] Y. Tan, H. Yu, Y. Li, C. Wu, J. Dong, J. Wen, Magnesium potassium phosphate cement prepared by the byproduct of magnesium oxide after producing Li_2CO_3 from salt lakes, *Ceramics International* 40(8) (2014) 13543-13551.
- [34] N. Dung, C. Unluer, Improving the performance of reactive MgO cement-based concrete mixes, *Construction and Building Materials* 126 (2016) 747-758.
- [35] L. Wang, L. Chen, J.L. Provis, D.C. Tsang, C.S. Poon, Accelerated carbonation of reactive MgO and Portland cement blends under flowing CO_2 gas, *Cement and Concrete Composites* 106 (2020) 103489.
- [36] N. Dung, C. Unluer, Development of MgO concrete with enhanced hydration and carbonation mechanisms, *Cement and Concrete Research* 103 (2018).
- [37] Q. Li, Y. Ding, G. Yu, C. Li, F. Li, Y. Qian, Fabrication of light-emitting porous hydromagnesite with rosette-like architecture, *Solid State Communications* 125(2) (2003) 117-120.
- [38] R. Zhang, N. Bassim, D.K. Panesar, Characterization of Mg components in reactive MgO–Portland cement blends during hydration and carbonation, *Journal of CO_2 Utilization* 27 (2018) 518-527.
- [39] P.J. Davies, B. Bubela, The transformation of nesquehonite into hydromagnesite, *Chemical Geology* 12(4) (1973) 289-300.
- [40] S. Ruan, J. Qiu, E.-H. Yang, C. Unluer, Fiber-reinforced reactive magnesia-based tensile strain-hardening composites, *Cement and Concrete Composites* 89 (2018) 52-61.
- [41] H.L. Wu, D. Zhang, B. Ellis, V. C. Li, Development of reactive MgO-based Engineered Cementitious Composite (ECC) through accelerated carbonation curing, *Construction and Building Materials* 191 (2018) 23-31.
- [42] N. Dung, C. Unluer, Carbonated MgO concrete with improved performance: The influence of temperature and hydration agent on hydration, carbonation and strength gain, *Cement and Concrete Composites* (2017).

- [43] S. Ruan, C. Unluer, Comparison of the environmental impacts of reactive magnesia and calcined dolomite and their performance under different curing conditions, *Journal of Materials in Civil Engineering* 30(11) (2018) 04018279.
- [44] S. Ruan, J. Liu, E.-H. Yang, C. Unluer, Performance and microstructure of calcined dolomite and reactive magnesia-based concrete samples, *Journal of Materials in Civil Engineering* 29(12) (2017) 04017236.
- [45] R. Zhang, D.K. Panesar, Mechanical properties and rapid chloride permeability of carbonated concrete containing reactive MgO, *Construction and Building Materials* 172 (2018) 77-85.
- [46] R. Zhang, D.K. Panesar, Design of carbonated r-MgO-PC binder system: Effect of r-MgO replacement level and water-to-binder ratio, *Journal of the American Ceramic Society* 103(1) (2020) 656-669.
- [47] K.R. Lauer, F.O. Slate, Autogenous healing of cement paste, *ACI Materials Journal* 52(6) (1956) 1083-1097.
- [48] S. Ruan, J. Qiu, Y. Weng, Y. Yang, E.-H. Yang, J. Chu, C. Unluer, The use of microbial induced carbonate precipitation in healing cracks within reactive magnesia cement-based blends, *Cement and Concrete Research* 115 (2019) 176-188.
- [49] D. Zhang, H. Wu, V.C. Li, B.R. Ellis, Autogenous healing of Engineered Cementitious Composites (ECC) based on MgO-fly ash binary system activated by carbonation curing, *Construction and Building Materials* 238 (2020) 117672.
- [50] H.-L. Wu, D. Zhang, Y.-J. Du, V.C. Li, Durability of Engineered Cementitious Composite exposed to Acid Mine Drainage, *Cement and Concrete Composites* (2020) 103550.
- [51] M. Sahmaran, G. Yildirim, T.K. Erdem, Self-healing capability of cementitious composites incorporating different supplementary cementitious materials, *Cement and Concrete Composites* 35(1) (2013) 89-101.
- [52] W. Ramm, M. Biscopig, Autogenous healing and reinforcement corrosion of water-penetrated separation cracks in reinforced concrete, *Nuclear Engineering and Design* 179(2) (1998) 191-200.

- [53] J. Qiu, S. Ruan, C. Unluer, E.-H. Yang, Autogenous healing of fiber-reinforced reactive magnesia-based tensile strain-hardening composites, *Cement and Concrete Research* 115 (2019) 401-413.
- [54] L. Mo, M. Deng, M. Tang, Effects of calcination condition on expansion property of MgO-type expansive agent used in cement-based materials, *Cement and Concrete Research* 40(3) (2010) 437-446.
- [55] S. Ruan, Development of reactive magnesia cement-based formulations with improved performance and sustainability. Doctoral thesis, Nanyang Technological University, Singapore, 2019.
- [56] S. Ruan, C. Unluer, Effect of air entrainment on the performance of reactive MgO and PC mixes, *Construction and Building Materials* 142 (2017) 221-232.
- [57] H. Liu, Q. Zhang, C. Gu, H. Su, V.C. Li, Influence of micro-cracking on the permeability of engineered cementitious composites, *Cement and Concrete Composites* 72 (2016) 104-113.
- [58] D.K. Panesar, L. Mo, Properties of binary and ternary reactive MgO mortar blends subjected to CO₂ curing, *Cement and Concrete Composites* 38 (2013) 40-49.
- [59] ASTM, C215-14. Standard test method for fundamental transverse, longitudinal, and torsional frequencies of concrete specimens, ASTM Committee C09, 2014.
- [60] T. Fukushima, Y. Yoshizaki, F. Tomosawa, K. Takahashi, Relationship between neutralization depth and concentration distribution of CaCO₃-Ca(OH)₂ in carbonated concrete, *Recent Advances in Concrete Technology*, 1998.
- [61] C.-F. Chang, J.-W. Chen, The experimental investigation of concrete carbonation depth, *Cement and Concrete Research* 36(9) (2006) 1760-1767.
- [62] R. Zhang, D.K. Panesar, Water absorption of carbonated reactive MgO concrete and its correlation with the pore structure, *Journal of CO₂ Utilization* 24 (2018) 350-360.
- [63] L. Mo, F. Zhang, M. Deng, F. Jin, A. Al-Tabbaa, A. Wang, Accelerated carbonation and performance of concrete made with steel slag as binding materials and aggregates, *Cement and Concrete Composites* 83 (2017) 138-145.

- [64] J. Qiu, W.L. Aw-Yong, E.-H. Yang, Effect of self-healing on fatigue of engineered cementitious composites (ECCs), *Cement and Concrete Composites* 94 (2018) 145-152.
- [65] S. Ruan, S. Liang, G. Kastiukas, W. Zhu, X. Zhou, Solidification of waste excavation clay using reactive magnesia, quicklime, sodium carbonate and early-age oven curing, *Construction and Building Materials* 258 (2020) 120333.
- [66] V.G. Papadakis, C.G. Vayenas, M.N. Fardis, Fundamental modeling and experimental investigation of concrete carbonation, *ACI Materials Journal* 88(4) (1991) 363-373.
- [67] S. Ruan, C. Unluer, Influence of mix design on the carbonation, mechanical properties and microstructure of reactive MgO cement-based concrete, *Cement and Concrete Composites* 80 (2017) 104-114.
- [68] M.P. Anisimov, Nucleation: theory and experiment, *Russian Chemical Reviews* 72(7) (2003) 591-628.
- [69] Mindess S., Young J. F., D. D, *Concrete* (2nd edition). Prentice Hall, Upper Saddle River, NJ, 2003.
- [70] G. Stephan, C.H. MacGillavry, The crystal structure of nesquehonite, $MgCO_3 \cdot 3H_2O$, *Acta Crystallographica Section B: Structural Crystallography and Crystal Chemistry* 28(4) (1972) 1031-1033.
- [71] L. Vandeperre, A. Al-Tabbaa, Accelerated carbonation of reactive MgO cements, *Advances in Cement Research* 19(2) (2007) 67-79.
- [72] S. Fan, M. Li, X-ray computed microtomography of three-dimensional microcracks and self-healing in engineered cementitious composites, *Smart Materials and Structures* 24(1) (2014) 015021.
- [73] V. Ferrini, C. De Vito, S. Mignardi, Synthesis of nesquehonite by reaction of gaseous CO_2 with Mg chloride solution: Its potential role in the sequestration of carbon dioxide, *Journal of Hazardous Materials* 168(2-3) (2009) 832-837.
- [74] Z. Zhang, Y. Zheng, Y. Ni, Z. Liu, J. Chen, X. Liang, Temperature- and pH-dependent morphology and FT-IR analysis of magnesium carbonate hydrates, *The Journal of Physical Chemistry B* 110(26) (2006) 12969-12973.

[75] M.C. Hales, R.L. Frost, W.N. Martens, Thermo-Raman spectroscopy of synthetic nesquehonite—implication for the geosequestration of greenhouse gases, *Journal of Raman Spectroscopy* 39(9) (2008) 1141-1149.

List of Tables

Table 1 Chemical composition (wt.%) of RMC and FA

Binder	MgO	CaO	SiO₂	Fe₂O₃	Al₂O₃	K₂O	TiO₂	Others
RMC	97.0	1.3	1.3	0.2	0.2	-	-	-
FA	0.8	1.2	58.6	4.7	30.4	1.5	2.0	0.8

Table 2 Physical properties of PVA fibers

Length (mm)	12
Diameter (μm)	39
Density (kg/m^3)	1300
Nominal tensile strength (MPa)	1600

Table 3 Mix design proportions (kg/m³) of RMC-based SHC samples prepared in this study

RMC	FA	Water	(NaPO₃)₆	PVA fibers
858	368	549	55	6.5

Table 4 RF ratios of samples with various crack widths before cracking and at different lengths of healing cycles, with respect to the original/unloaded samples

Average crack width (μm)	Original/unloaded RF	RF ratios at different healing cycles					
		RF ₀	RF ₂	RF ₄	RF ₆	RF ₈	RF ₁₀
23.4	1004	106%	105%	110%	108%	109%	110%
30.2	966	104%	115%	117%	119%	120%	118%
32.1	1019	87%	99%	104%	105%	110%	109%
37.7	999	94%	101%	113%	114%	115%	115%
38.1	1086	92%	97%	106%	106%	106%	106%
63.4	1062	99%	105%	105%	105%	105%	105%
64.9	1026	87%	111%	106%	105%	105%	104%
69.8	1092	91%	101%	102%	101%	101%	101%
70.7	1039	85%	91%	96%	101%	102%	102%
71.1	1077	85%	91%	100%	101%	101%	101%
74.7	1039	98%	107%	107%	107%	107%	107%
75.7	1057	87%	110%	109%	108%	109%	108%
78.8	1013	84%	94%	100%	103%	107%	107%
79.7	1072	82%	105%	100%	101%	102%	102%
79.8	1079	84%	101%	100%	102%	102%	103%
83.6	1121	77%	86%	90%	100%	100%	100%
88.2	1011	98%	102%	101%	102%	105%	105%
96.7	1082	89%	103%	106%	105%	105%	106%
112.3	1105	78%	88%	94%	91%	94%	96%
118.0	1082	68%	86%	97%	99%	96%	102%
120.8	1085	78%	109%	105%	103%	103%	103%

List of Figures

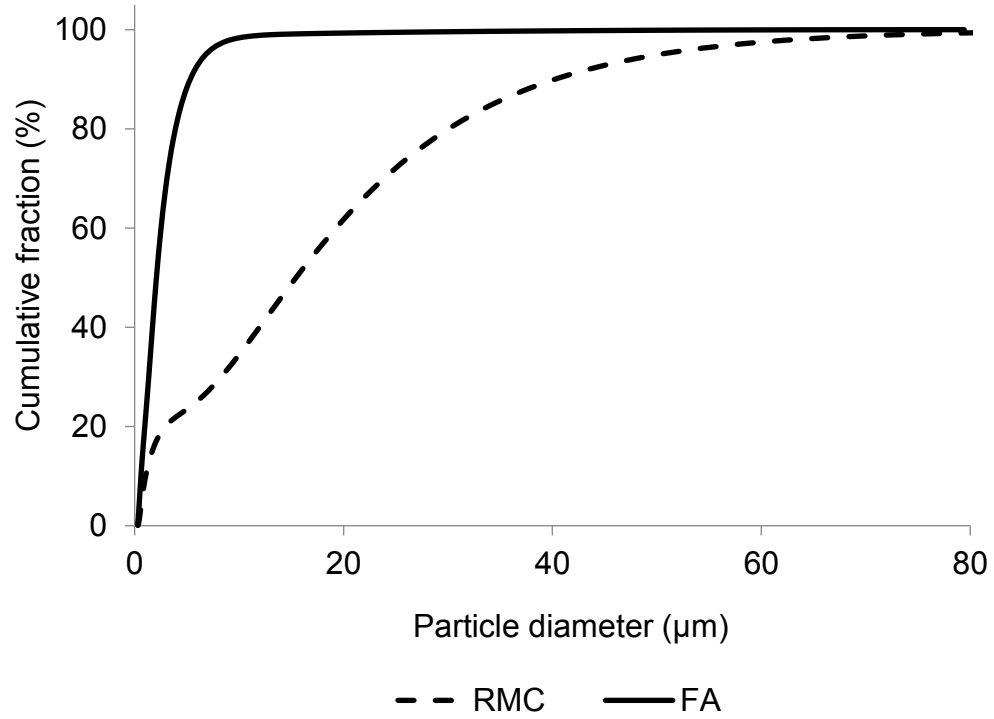
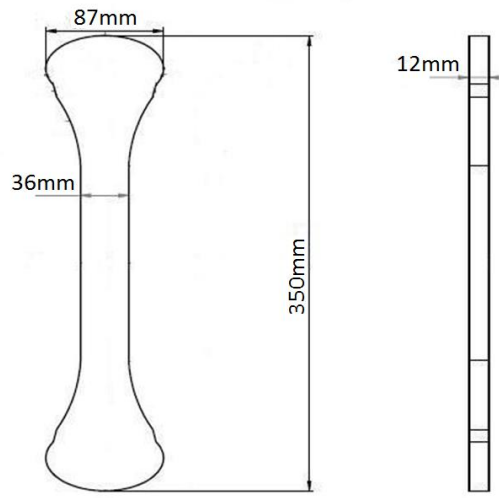


Fig. 1 Particle size distribution of RMC and FA



Fig. 2 Morphology of PVA fibers used in this study



(a)



(b)

Fig. 3 Illustration of the uniaxial tensile test, showing (a) the dimensions of the dog-bone specimens and (b) the test setup

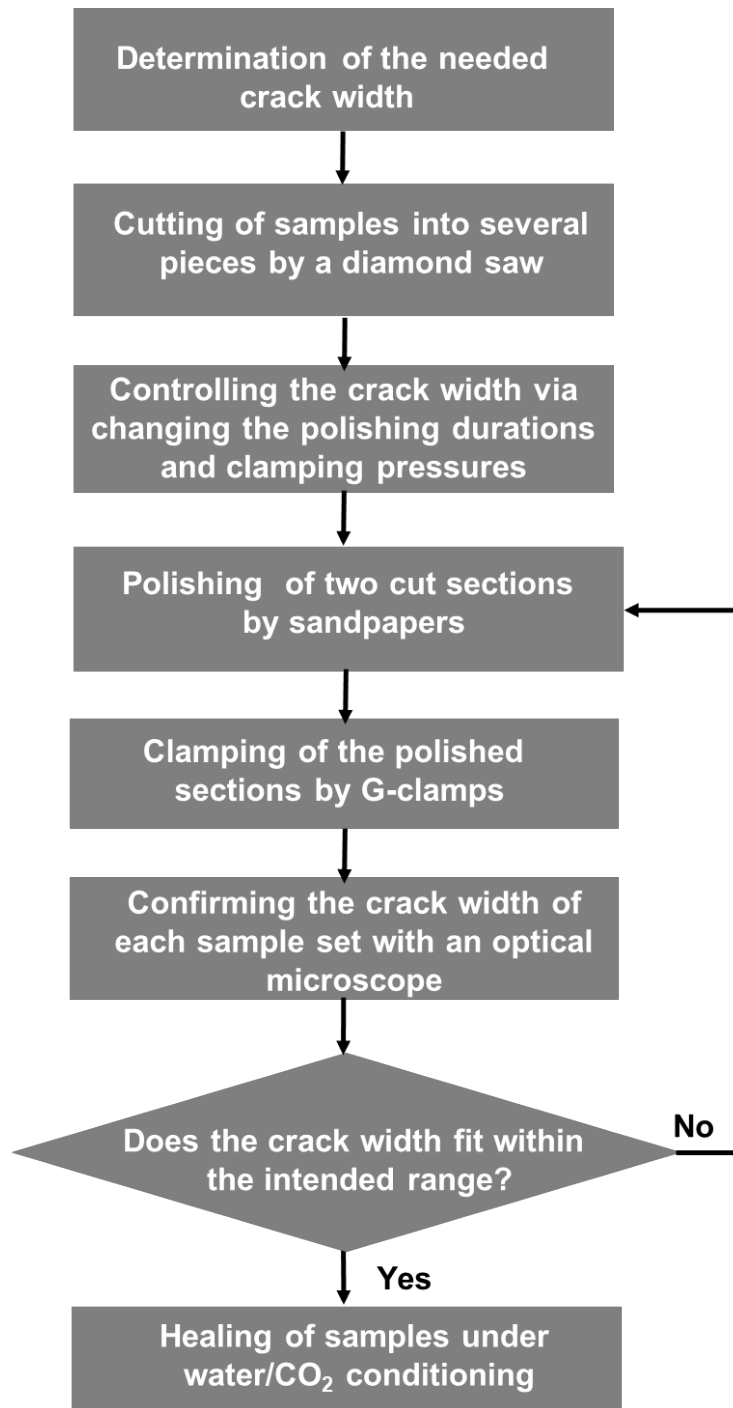


Fig. 4 Flow chart showing the steps involved in the preparation of samples with controlled crack widths

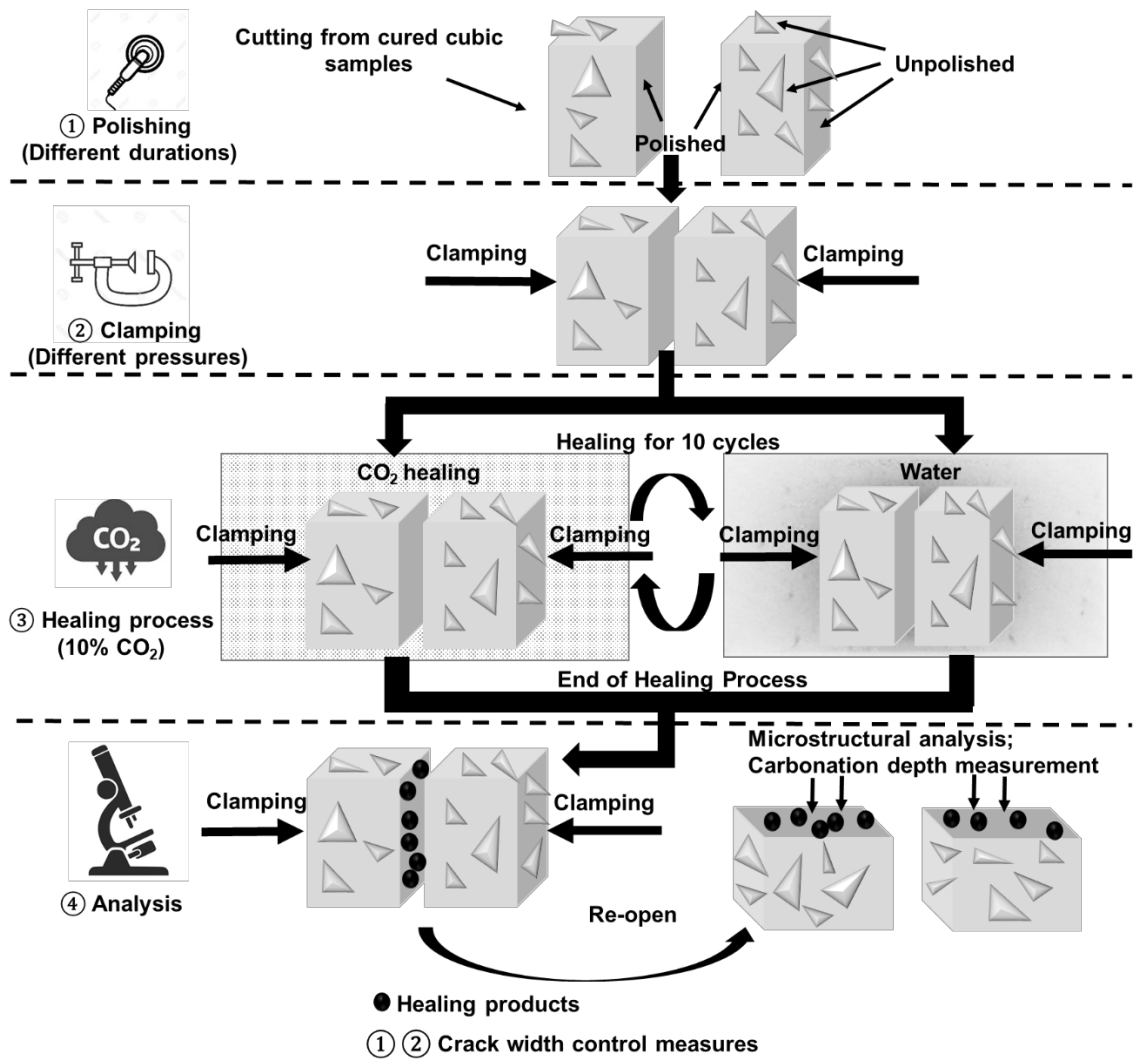


Fig. 5 Representation of the healing process and the exposure of the final healing products for microstructural analysis and carbonation depth measurements

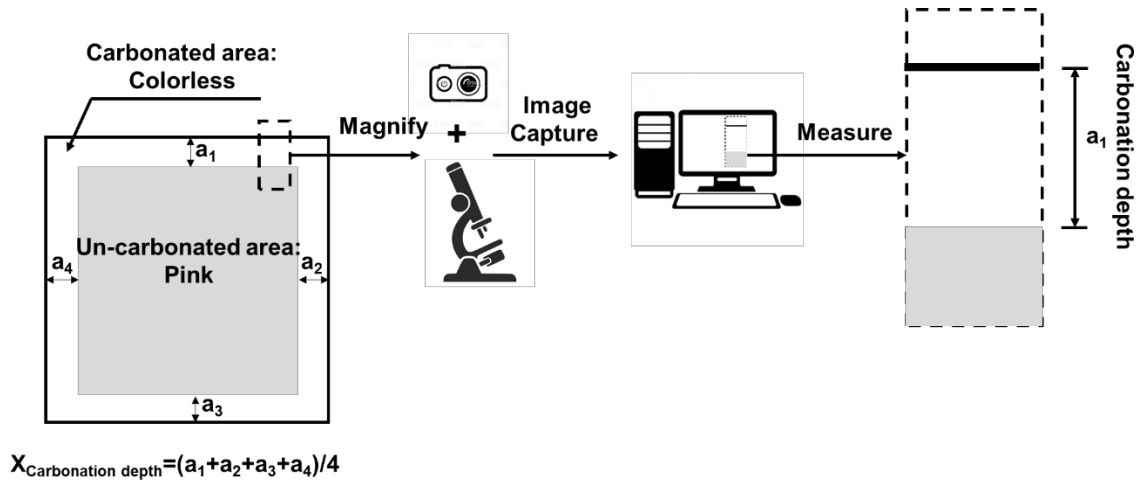
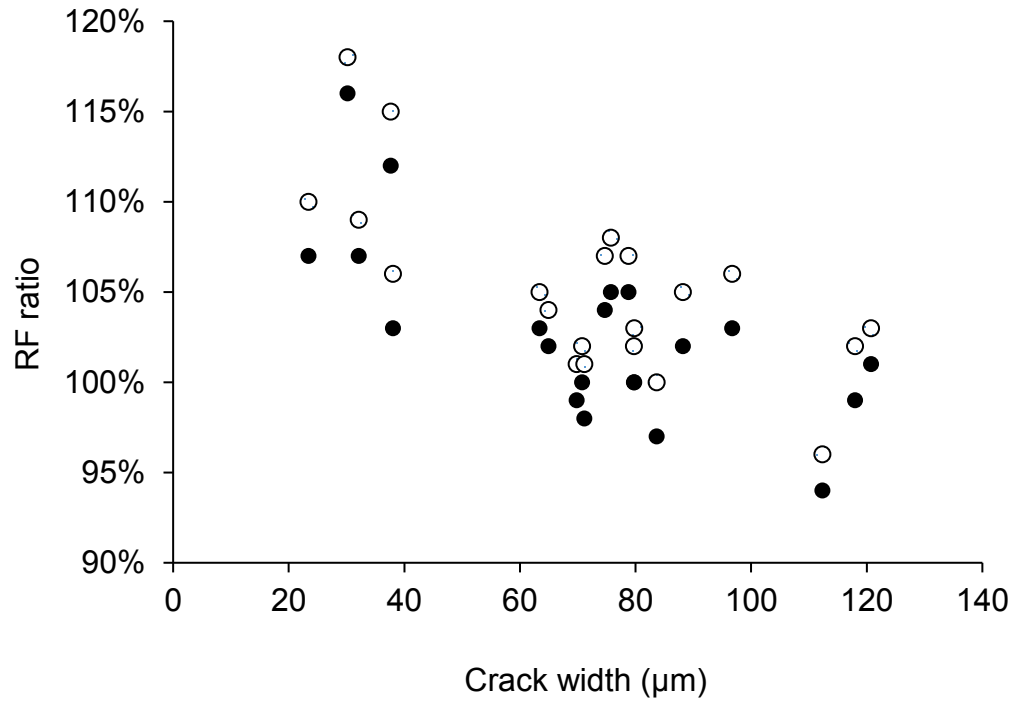


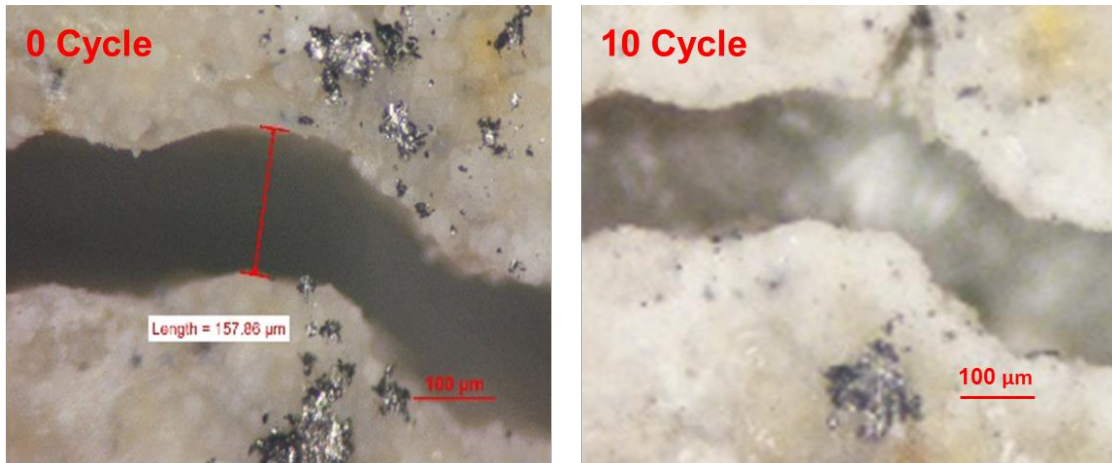
Fig. 6 Illustration of the measurement of carbonation depth in RMC-based samples



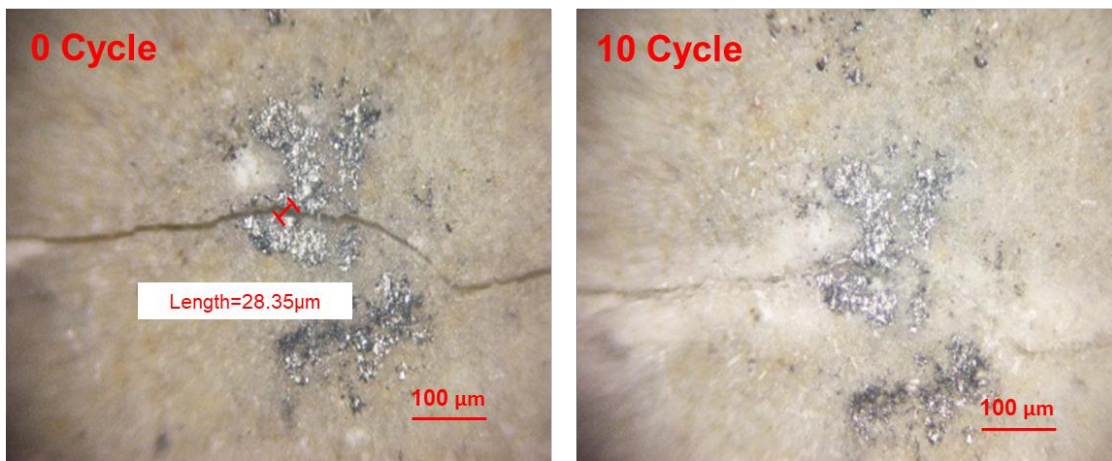
- Normalized with respect to the original samples
- Normalized with respect to the control samples

Note: The points located at (79.71μm, 100%) and (79.79 μm, 100%) overlap in the figure as the values are very close.

Fig. 7 RF ratios of samples (i.e. normalized with respect to the original and control samples) subjected to CO₂/water conditioning for up to 10 cycles



(a) $>100 \mu\text{m}$



(b) $<100 \mu\text{m}$

Fig. 8 Progress of healing within the cracks of samples subjected to CO₂/water conditioning, showing different forms of healing identified as (a) internal healing and (b) mixed healing

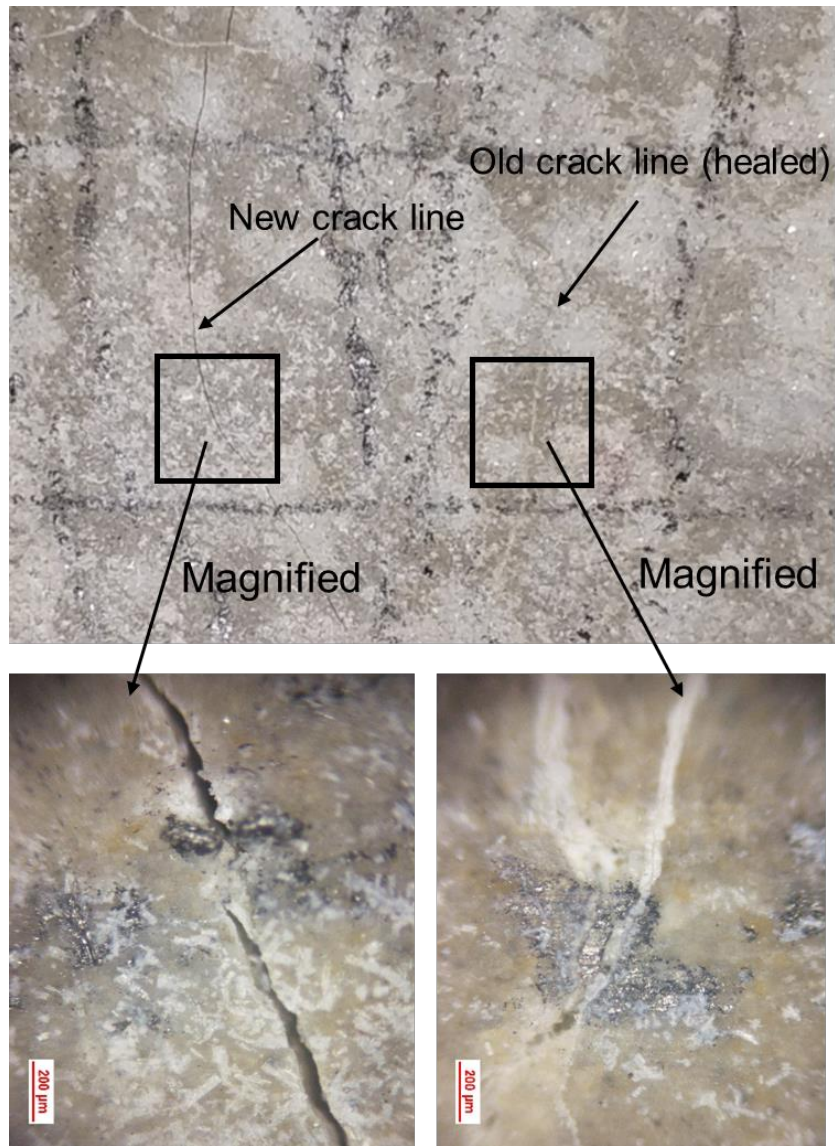


Fig. 9 Formation of new cracks within healed samples subjected to reloading after 10 cycles of healing under CO₂/water conditioning

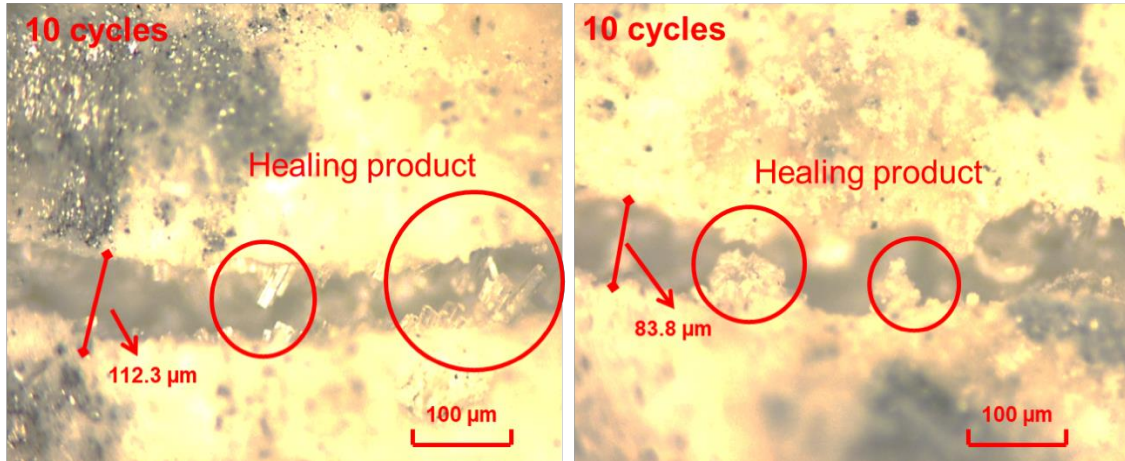
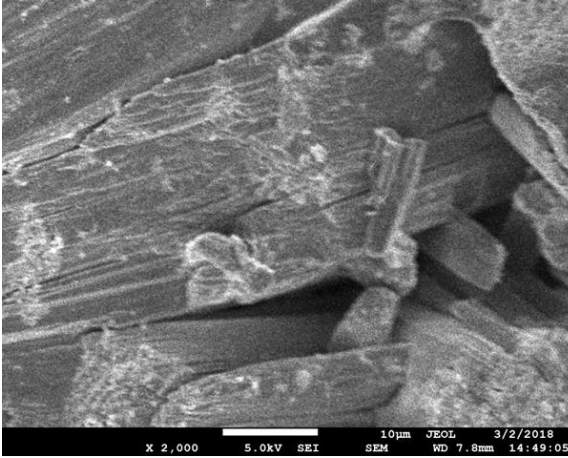
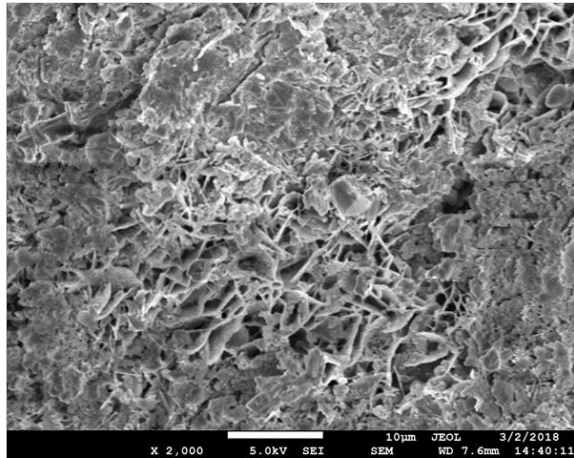


Fig. 10 Morphologies of the crystals that formed within cracks of different widths observed under optical microscopy after 10 cycles of healing under CO₂/water conditioning

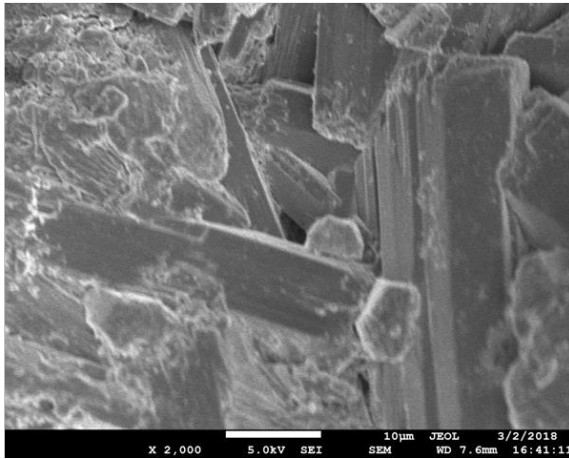


(a1)

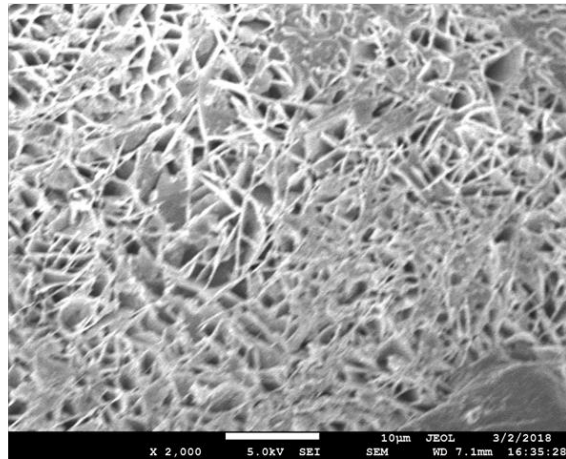


(a2)

(a)

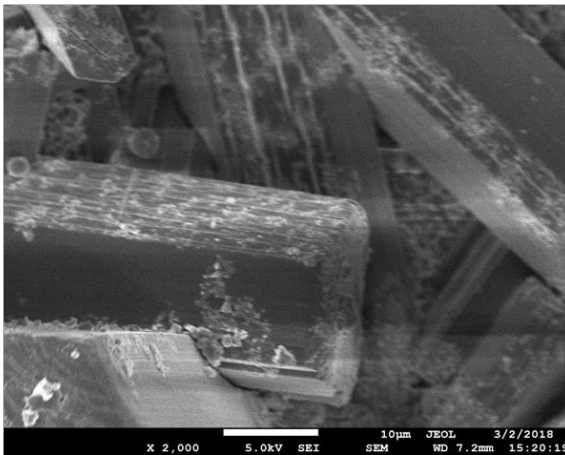


(b1)

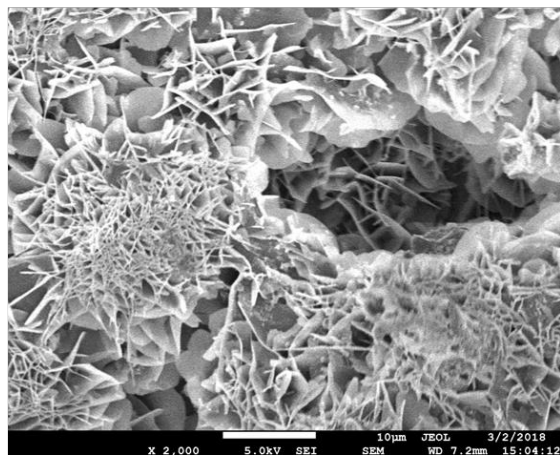


(b2)

(b)



(c1)



(c2)

(c)

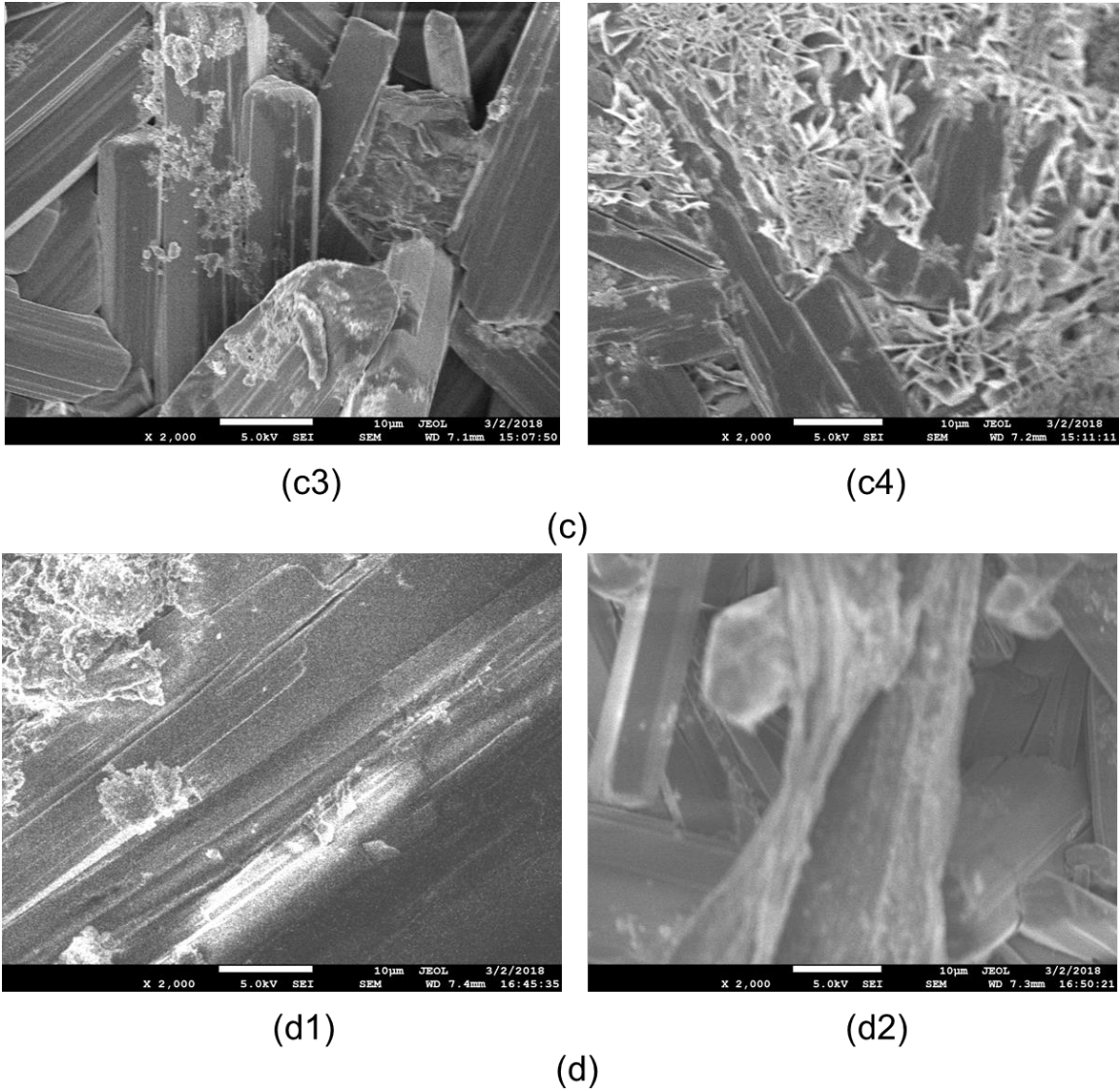
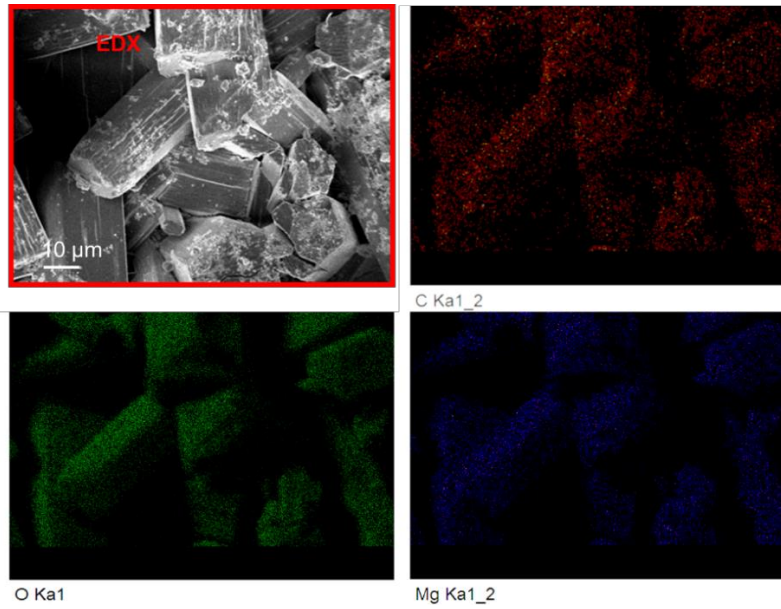
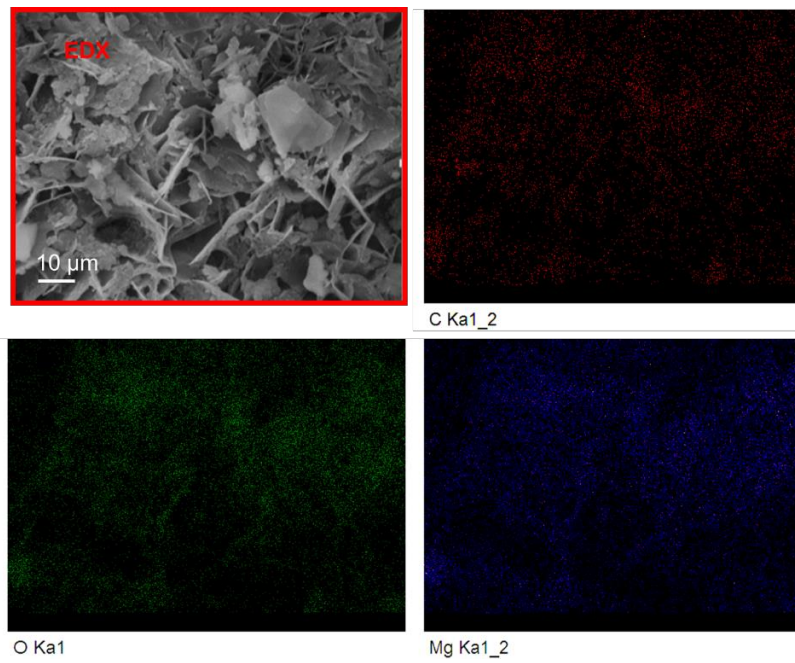


Fig. 11 Microstructural images of the healing products that formed at the edges (a1, b1, c1, d1) and internal sections (a2, b2, c2, c3, c4, d2) of cracks with different widths after 10 cycles of healing under CO₂/water conditioning (a: < 50 μm; b: 50-100 μm; c: 100-150 μm; d: > 200 μm)



(a)



(b)

Fig. 12 Elemental mapping of the healing products that formed at the (a) edges and (b) inner sections of cracks after 10 cycles of healing under CO₂/water conditioning

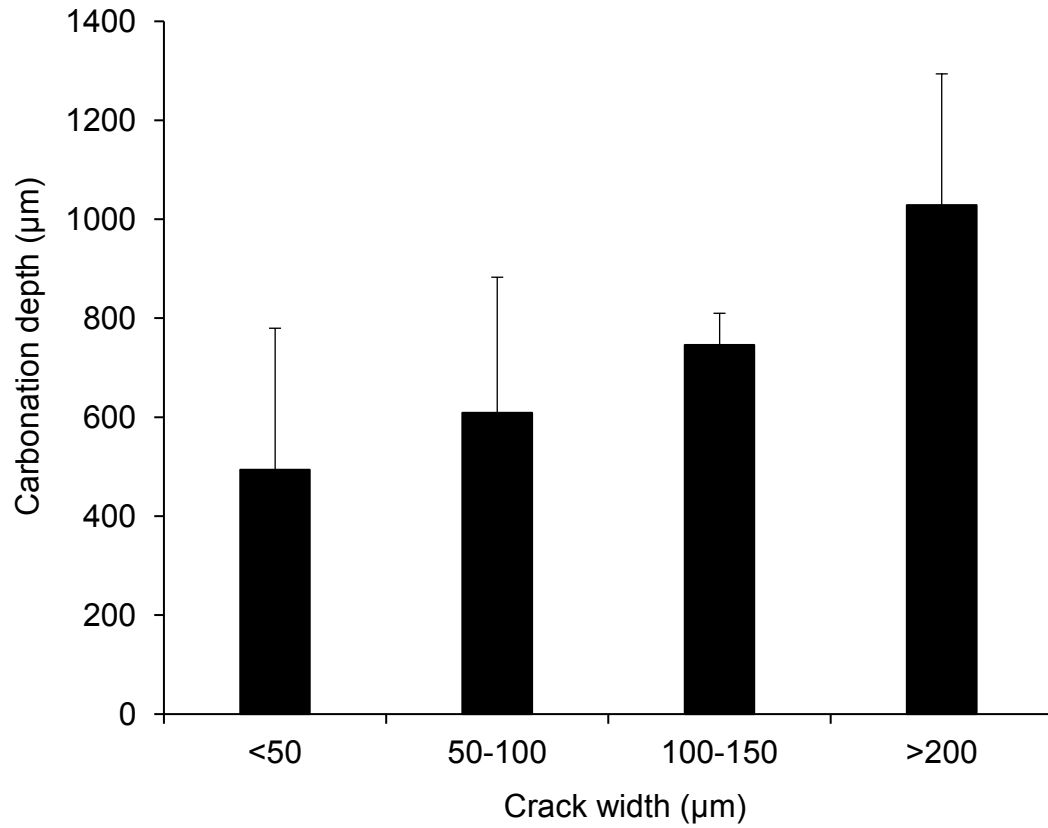


Fig. 13 Carbonation depths of samples with different crack widths after 10 cycles of healing under CO₂/water conditioning

